PAPER

Check for updates

One-step generation of S and N co-doped reduced graphene oxide for high-efficiency adsorption towards methylene blue†

Meixiu Li,[ab] Yanhui Li, [ID] *[ab] Xiaoping Zhang,[c] Heng Zheng,[a] Aitang Zhang,[a] Tao Chen,[a] Wenhao Liu,[d] Yuanhai Yu,[b] Jingquan Liu, [ID] [a] Qiuju Du,[a] Dechang Wang[b] and Yanzhi Xia[a]

S and N co-doped reduced graphene (S–N–rGO) nanohybrids were prepared by a one-step oil bath heating process using glutathione (GSH) as a green and mild co-reduction agent and a S and N source. It can be applied in the field of adsorption for the removal of methylene blue (MB) from aqueous solutions. The efficient adsorption rate of S–N–rGO hybrids for MB (50 mg L^{-1}) was observed with the best even within 2′07″ from blue solutions into colorless (the mass ratio GO : GSH = 60 : 200). Under this mass ratio, the effects of initial solution pH, temperature, initial concentration and contact time on adsorption towards MB were explored systematically. The results indicated that the adsorption capacity at 275 K could reach up to 598.8 mg g^{-1}, the adsorption behavior followed the pseudo-second-order kinetic model and the equilibrium adsorption data fitted the Langmuir isotherm well. Thermodynamic and kinetic analyses revealed that adsorption is an exothermic, spontaneous and physisorption process.

1. Introduction

With the development of science and technology and the growing demand for materials, different kinds of industries including food, leather, textile, plastic, cosmetic, paper, printing and dye continue to expand. However, the problem of water contamination caused by dye industries need to be addressed urgently. At present, the methods used for removing dyes from water can be divided into three main types: physical, chemical and biological means. In addition, high cost, and low removal efficiency and secondary pollution are the main challenges to remove dyes from wastewater. Compared with others, the best advantage of physical methods is easy operation. Adsorption, membrane separation, magnetic separation, extraction and leach are frequently used physical methods. Among them, the adsorption method has attracted increasing

attention due to its characteristics such as economy, high efficiency and easy operation.[1]

Compared with natural materials including zeolite, silica, wheat shells, orange peel, coir pith, almond shells and natural polymeric materials, synthetic nanomaterials have advantages due to their controllability of micromorphology and designability of chemical composition and surface groups.[2,3] With large specific surface area and easily modified surface groups, graphene and graphene-based materials have been widely applied in sewage treatment.[4–9] There are two methods to design the chemical composition of graphene: the surface functionality and heteroatom doping, which can provide active adsorption sites.[10–15] The results show that modifications are in favor of improvements of adsorption capacity of graphene towards dyes. For instance, Zhong's group[4] prepared a rhamnolipid-functionalized graphene oxide hybrid with abundant functional groups and mesopores feature by one-step ultrasonication. The adsorption capacity onto methylene blue (MB) of this hybrid calculated from the Langmuir model was 529.10, 568.18 and 581.40 mg g^{-1} at 298, 308 and 318 K, respectively, and it took more than 7 h to reach equilibrium for MB adsorption (200 mg L^{-1}, 298 K). In addition, graphene–Fe_3O_4@carbon (GFC) hybrids with hierarchical nanostructures were synthesized after treatments by one-pot solvothermal and hydrothermal carbonization processes,[10] which were applied for the adsorption of MB. Compared with the corresponding binary hybrids (graphene/Fe_3O_4 and Fe_3O_4@carbon), the adsorption capacity showed about 40% improvement and the dye removal efficiency of this hybrid could be retained at about 86% and

[a]*College of Materials Science and Engineering, State Key Laboratory of Bio-Fibers and Eco-Textiles, Collaborative Innovation Center for Marine Biomass Fibers Materials and Textiles of Shandong Province, Qingdao University, Qingdao 266071, China. E-mail: liyanhui537@163.com*

[b]*College of Mechanical and Electrical Engineering, Qingdao University, Qingdao 266071, China*

[c]*College of Textile and Clothing, Qingdao University, 308 Ningxia Road, Qingdao 266071, China*

[d]*School of Mechanical Engineering and Automation, University of Science and Technology Liaoning, Liaoning 114051, China*

77% after five adsorption–desorption cycles in water and 1 M HCl, respectively. Although the equilibrium for MB (50 mg L^{-1}, 298 K) was reached within 20 min, the adsorption capacity of these hybrids was not more than 50 mg g^{-1}. In these studies, both adsorption rates and capacities of adsorbents are not simultaneous and significantly improved, and the reality is that the rate of production of sewage is much faster than that at which it can be treated. For heteroatom doping, S, B, P and N are the main heteroatoms. The results indicated that co-doping of S and N can improve the reactivity and their potential applications[15–17] Several methods such as hydrothermal[18–20] or solvothermal[21] method, chemical vapour deposition,[22] reflux[23] and thermal annealing[24,25] were developed to prepare S and N co-doped graphenes. Ci's group[26] prepared S and N co-doped graphene aerogel using thiourea as a S and N source to adsorb radioiodine in nuclear waste with a maximum iodine adsorption capacity up to 999 mg g^{-1} at 298 K. Feng and his coworkers investigated the adsorption performance of S and N co-doped graphene hydrogels onto malachite green. It was found that the maximum adsorption was 740.7 mg L^{-1} after more than 100 min to reach equilibrium at 293 K. High cost is the main challenge limiting their applications. Therefore, developing a facile route for the synthesis of the modified graphene that has high adsorption rate and large adsorption capacities towards dyes is still in great demand.

Herein, we report a facile strategy to directly synthesize S and N co-doped reduced graphene oxide (denoted as S–N-rGO) by one-step oil bath heating method in the presence of glutathione (GSH) as a mild reducing agent. After preparation by an environment-friendly, simple process, S–N-rGO hybrids were obtained, and the effects of the amount of GSH, initial solution pH, temperature, initial concentration and contact time on the adsorption of MB were studied by batch adsorption experiments. In addition, the equilibrium, kinetics, thermodynamics and adsorption mechanism of adsorption processes were also further investigated.

2. Experimental section

2.1 Materials

Natural graphite powder (99%) with an average size of 3 mm was supplied by Xiamen Knano Graphite Technology Co., Ltd. GSH (99%, BR) was purchased from Shanghai Yuanye Co., Ltd. Sulfuric acid (98%, AR), potassium permanganate (99%, AR), sodium nitrite (99%, AR) and hydrogen peroxide (30%, AR) were purchased from Shanghai Jinlu Chemical Co., Ltd. MB was provided by Tianjin Red Cliff Chemical Reagent Factory. All reagents were used without further purification.

2.2 Synthesis of S–N-rGO

The graphene oxide (GO) was synthesized according to a modified Hummers method as previously described in the literature.[27] The as-prepared GO was purified by dialysis in double-distilled water for three days using a 3500 Da cut-off dialysis membrane tube. The stable GO suspension (1.2 mg mL^{-1}) was obtained by sonication under ambient conditions for 1 h.

First, GSH (200 mg, 4 mmol) was added to the freshly prepared suspension of GO (1.2 mg mL^{-1}, 50 mL) under mechanical stirring for 10 min. After that, the reaction mixture was transferred to a beaker and treated at 90 °C for 11 h in an oil bath. The as-synthesized product was collected by centrifugation and washed several times with deionized water to afford the S and N co-doped rGO (S–N-rGO) aqueous suspension, which was freeze-dried for subsequent use. For comparison, rGO was prepared using the same procedures, but without the addition of GSH.

2.3 Instruments

Scanning electron microscopy (SEM, FEI Quanta200F) was performed to analyze the morphology of S–N-rGO. SEM mapping (JEM-2100F) was carried out to characterize the distribution of the elements. The physical structures and chemical compositions of the as-synthesized S–N-rGO were characterized by X-ray diffraction (XRD, X'Pert-PRO MPD and MRD, PANalytical, Holland), X-ray photoelectron spectroscopy (XPS, ESCALAB 250XI), Raman spectroscopy (Jobin-Yvon HR 800 France), and Fourier transform infrared (FTIR) spectroscopy (Tensor 27, Bruker Corporation).

2.4 Bath adsorption experiments

The MB (1000 mg L^{-1}) stock solution was prepared by dissolving MB in deionized water; different desired concentrations of MB were obtained by diluting the stock solution during the experiment. Adsorption experiments were carried out in 50 mL glass conical flasks containing 20 mL of different dye concentrations and 10 mg adsorbents. All samples were placed in a water bath shaker (SHZ-82A) and shaken to equilibrium at room temperature (294 K). The equilibrium concentration of MB in the solution was determined using a UV-Vis spectrophotometer (TU-1810, Beijing Purkinje General Instrument Co., Ltd., Beijing) after adsorption. The MB adsorption amount q_e (mg g^{-1}) was calculated using the following formula:

$$q_e = \frac{(c_0 - c_e)}{M} \times V \tag{1}$$

where c_0 and c_e are the initial and equilibrium concentrations (mg L^{-1}) of MB in the solution, V is the volume of the solution (L), and M is the mass (g) of the adsorbent used.

The effect of dose on MB adsorption onto S–N-rGO was determined by adding different amounts of S–N-rGO (5–25 mg) to 20 mL solution with an MB concentration of 240 mg L^{-1}.

The effect of pH on adsorption was determined by adding 10 mg S–N-rGO into 20 mL solution with an MB concentration of 240 mg L^{-1}. The solution pH was adjusted from 4 to 10 using a HNO$_3$ or NaOH solution.

The effect of contact time on dye removal was investigated by adding 100 mg adsorbents into 200 mL solution with an MB concentration of 240 mg L^{-1}. At a predetermined time interval, the MB concentration of the solution was measured using an UV-Vis spectrophotometer and the adsorption capacity q_t (mg g^{-1}) at time t can be obtained using the following equation:

$$q_t = \frac{(c_0 - c_t)}{M} \times V \qquad (2)$$

where c_t (mg L^{-1}) is the residual concentration of MB at time t.

The effect of temperature on adsorption was investigated by adding 10 mg adsorbents into 20 mL solutions with MB concentrations ranging from 200 to 300 mg L^{-1} at 275, 294, and 313 K, respectively. Except for experiments that investigated the effect of contact time (202 min), the reaction time of the above-mentioned experiments was 150 min.

3. Results and discussions

3.1 Characterization of S–N-rGO

The morphology of the as-prepared S–N-rGO was first characterized by SEM and SEM mapping. As shown in Fig. 1A–C, compared with the lamellar structure with less wrinkles of rGO, the rGO nanosheets of S–N-rGO exhibited obvious aggregations with many wrinkles. The SEM mapping technique was also adopted to visualize the distribution of the elements of S–N-rGO (Fig. 1D). It can be seen that elements of C, N, O and S were uniformly distributed on the surface of rGO, where S and N come from the mercapto groups and amido bonds of GSH, respectively.

The phase information of S–N-rGO was investigated by XRD (Fig. 2A). It can be observed that the diffraction peak at about 25° was assigned to (002) of rGO, which indicated the successful reduction of GO into rGO by GSH. In addition, the weak diffraction peaks at 2θ degrees of 19.6°, 23.6°, 27.3°, 31.0°, 39.0°, 41.0° and 42.5° could be assigned to the sulfur nitride (JCPDS card no. 36-0535), which confirmed the presence of S and N consistent with the SEM mapping.

The chemical states of S–N-rGO were further analyzed by XPS, and the results are shown in Fig. 2B–D. Obviously, the N, O, S and C elements all existed. In addition, the result showed that the atomic percentage of C, N, O and S was 69.67%, 10.73%, 15.55% and 4.05%, respectively. The deconvoluted high-resolution N 1s spectrum of S–N-rGO is shown in Fig. 2C. Generally, there are two N-containing functional groups in S–N-

rGO, which can be identified by the bonding state of the N atom. The peaks at 400.0 and 401.9 eV could correspond to the binding energies of pyrrolic N and quaternary N, respectively.[28–30] Besides, Fig. 2D exhibits the high-resolution S 2p spectrum of S–N-rGO. There were two peaks at the binding energies of 163.78 and 164.88 eV, which were in agreement with the reported S 2p$_{3/2}$ and S 2p$_{1/2}$ spectra attributed to sulfur binding in the C–S bonds and the conjugated –C=S– bonds, respectively.[31,32] The formation of C–S may be due to the reaction between oxygen-containing groups in GO and GSH and the –C=S– bonds could arise from the presence of a sulfur-based ring system, which indicated successful doping of S.

As shown in Fig. 2E, two characteristic peaks of graphenes could be observed for GO, rGO and S–N-rGO: the D band at 1349 cm^{-1} and the G band at 1598 cm^{-1}, respectively. The D band could be caused by defects in the graphene sheets and the G band could be attributed to the tangential vibrations of sp^2 bonded carbon atoms.[33] The I_D/I_G value of S–N-rGO was calculated to be 1.21, which was much higher than that of rGO (0.98) and GO (0.92) due to the introduction of S and N. FTIR spectroscopy was employed to characterize the carbon species in S–N-rGO and GO. As shown in Fig. 2F, compared with GO, S–N-rGO exhibited similar absorption peaks at 3345 cm^{-1}, 1627 cm^{-1} and 1384 cm^{-1}, which could correspond to the stretching vibration of the hydroxyl group, C=C skeletal vibration and C–O stretching vibration, respectively.[34–36] It is noteworthy that the absorption peaks appeared at 1646 cm^{-1} of S–N-rGO, which could be attributed to amide bonds[37] indicating that the reaction between GSH and GO occurred. Besides, the peak intensity of C=O at 1715 cm^{-1} in S–N-rGO was significantly increased due to the introduction of GSH.

3.2 Effects of operating conditions on MB adsorption

3.2.1 Effect of the amount of GSH. The adsorption behaviors of S–N-rGO hybridized with different amounts of GSH were evaluated by the rate of adsorption towards MB (50 mg L^{-1}). It can be seen from Table 1 that, apparently, the more the amount of GSH hybridized, the less the reaction time required for the adsorption of MB from blue solutions turning colorless with the
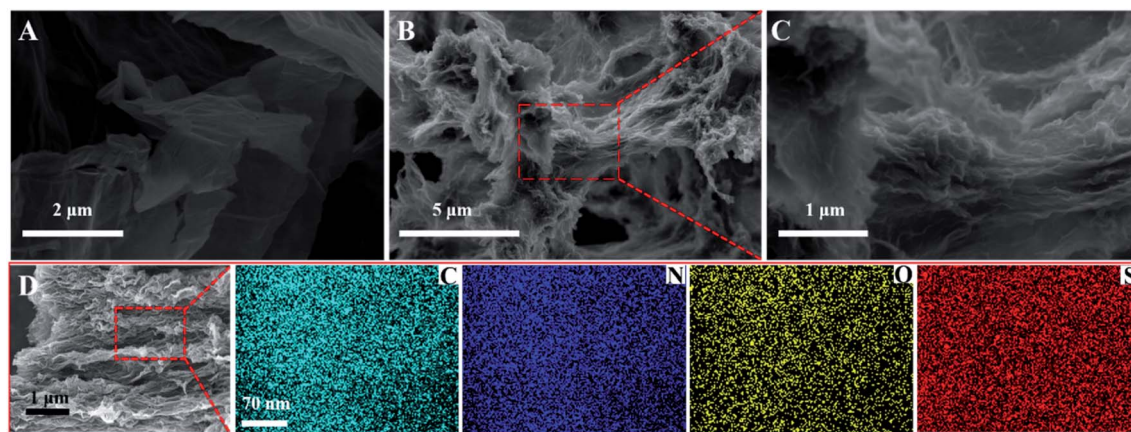

Fig. 1 SEM images of (A) GO and (B and C) S–N-rGO. (D) Elemental mappings of C, N, O and S of S–N-rGO.
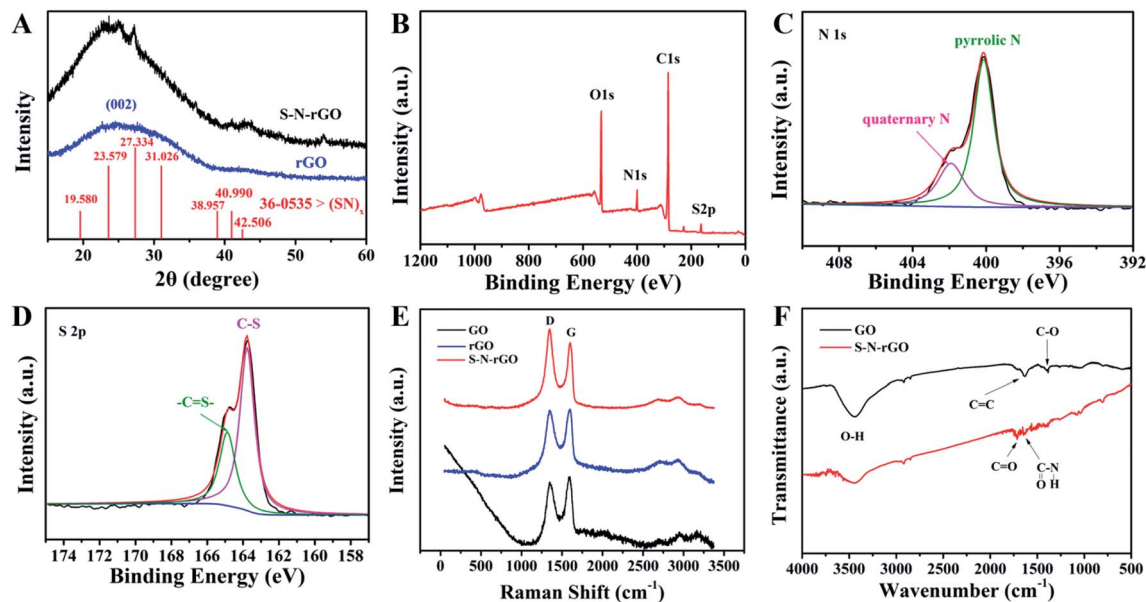
Fig. 2 (A) XRD patterns for S–N-rGO and rGO. (B) XPS broad spectrum and XPS survey scan of (C) N 1s and (D) S 2p for S–N-rGO. (E) Raman spectra of GO, rGO and S–N-rGO. (F) FTIR spectra of GO and S–N-rGO.

amount of hybridized GSH ranging from 0 to 200 mg. It may be due to the more active adsorption sites formed by doping of S and N on the surface of the graphene sheet with the increase in amount of GSH. In addition, the rate of adsorption was increased but not obvious when the amount of hybridized GSH was more than 200 mg, which was probably caused by the saturation of doping, and more active adsorption sites cannot be provided. Therefore, the best mass ratio between GO and GSH was determined to be 60 : 200, and other factors that effected MB adsorption were also evaluated under this condition. The detailed video of this sample adsorption towards MB

is provided in the ESI.† Besides, it can be found that there was no obvious difference in the adsorption capacities of every sample.

3.2.2 Effects of initial solution pH, dose, temperature and contact time. The effects of initial solution pH on MB (240 mg L^{-1}) adsorption onto S–N-rGO were studied within the pH range between 4 and 10 at room temperature (294 K), as shown in Fig. 3A. The adsorption capacities of MB presented an increasing trend from 473.90 to 479.90 mg g^{-1} with the increase in pH values in the range of 4–10. In addition, the MB removal efficiency can reach up to 99.98% when the initial pH of the MB
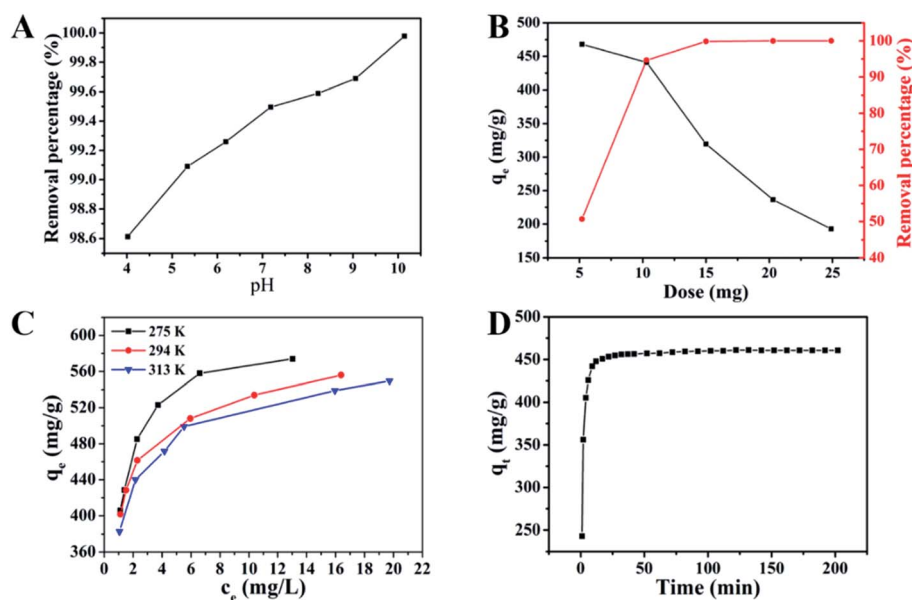

Fig. 3 Effect of different experimental parameters on adsorption of MB onto S–N-rGO: (A) pH, (B) dose, (C) temperature and (D) contact time.

Table 1 Time taken for the adsorption of MB from blue solutions turning into colorless among different mass ratios between GO and GSH

The mass ratio (GO : GSH)	60 : 0	60 : 50	60 : 100	60 : 150	60 : 200	60 : 250	60 : 300	60 : 350
Required time	10′16″	6′01″	4′56″	2′45″	2′07″	2′09″	2′10″	2′08″
Adsorption capacity (mg g^{-1})	96.8	94.5	99.5	95.0	99.3	94.8	94.7	95.1

solution is 10. In addition, it is noteworthy that all removal efficiencies were more than 98% even in the solution with pH 4 (98.73%) and suggested that S–N-rGO can be a high-efficiency adsorbent for the adsorption of MB and basic solutions favored MB adsorption. However, the adsorption capacities just increased by 1.26%. Therefore, the pH cannot be regarded as a factor affecting the adsorption process on account of a property of cationic dye of MB. High removal efficiencies may be attributed to the π–π stacking interactions between S–N-rGO and MB.[1]

Fig. 3B shows the effect of dose on MB adsorption. It can be clearly seen that the removal percentage increased rapidly from 50.68% to 99.85% with the increase in amount of adsorbent ranging from 5 to 15 mg and after that there was no obvious change until the amount of adsorbent was 25 mg. This could be ascribed to the more amount of adsorbents; more active sites are provided at the beginning, however, abundant adsorption sites are useless for saturated adsorption in the last second adsorption solutions.[38] At the same time, the adsorption capacity of S–N-rGO decreased because of the decrease in the number of adsorbents per unit weight of MB and the reduction in the utilization rate of active sites with the increase dose.[39]

Generally, the temperature has a significant effect on the diffusion rate of dye molecules and surface physicochemical properties of adsorbents. In order to study the role of temperature in the adsorption process of MB, adsorption experiments of S–N-rGO towards MB were investigated at different concentrations of MB (200–300 mg L^{-1}) and temperatures of 275, 294 and 313 K, as shown in Fig. 3C. It can be seen that the higher the concentration of MB, the bigger the adsorption capacity exhibited at the same temperatures, which could be attributed to the enhanced driving force of the concentration gradients with the increase in the dye concentration. Besides, it can be found that the adsorption capacity decreased with the increase in temperature under the same concentration of MB, which indicated that this adsorption was an exothermic process.

Fig. 3D shows the effect of contact time on the adsorption capacity of MB (240 mg L^{-1}) at 294 K onto S–N-rGO. It can be clearly seen that there was a sharp increase in the adsorption rate of MB on the initial 6 min and a fast increase from 9 min to 32 min, and the adsorption capacities at 6 and 9 min are 425.78 and 441.96 mg g^{-1}, respectively. After that, the adsorption rate becomes low and finally reaches the adsorption equilibrium. A change in the adsorption rate can be observed because there were more adsorption sites in the initial stage and less adsorption sites can be utilized with the increase in time.[40]

3.3 Adsorption isotherms

The adsorption mechanism and interactive behaviors between MB and S–N-rGO were studied by the adsorption isotherm. The equilibrium adsorption data were commonly analyzed by the Langmuir and Freundlich models. The first assumes that the adsorption occurs on the medium surface where the adsorption sites are evenly distributed and no interaction occurred between adsorbed dye molecules. The Langmuir equation is described as follows:[41]

$$\frac{c_e}{q_e} = \frac{c_e}{q_{max}} + \frac{1}{q_{max}K_L} \tag{3}$$

where c_e (mg L^{-1}) and q_e (mg g^{-1}) are the equilibrium concentration and equilibrium adsorption capacity, respectively.

The Langmuir constant k_L (L g^{-1}) and the maximum adsorption capacity q_{max} (mg g^{-1}) were determined by plotting c_e/q_e with respect to the straight line of c_e (Fig. 4A), and the results are presented in Table 2. The high determination coefficients R^2 demonstrated that the adsorption equilibrium of MB by S–N-rGO can be well described by the Langmuir model and the maximum monolayer capacity of S–N-rGO was 598.8 mg g^{-1}.

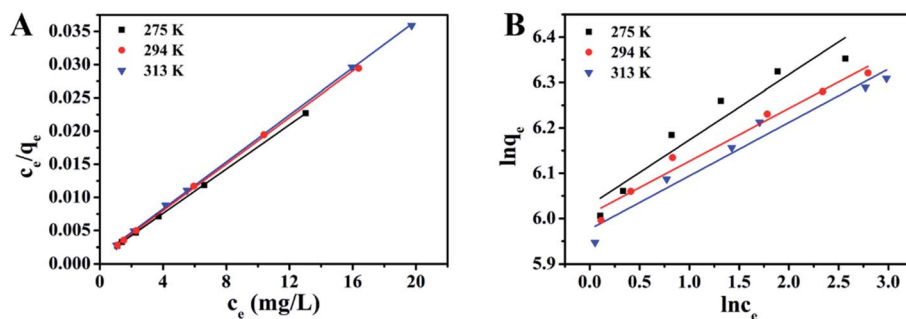Another equilibrium parameter R_L is defined as follows:[42]

Fig. 4 (A) Langmuir and (B) Freundlich isotherms for the adsorption of MB onto S–N-rGO.

Table 2 Adsorption isotherm model parameters for MB absorbed by S–N-rGO

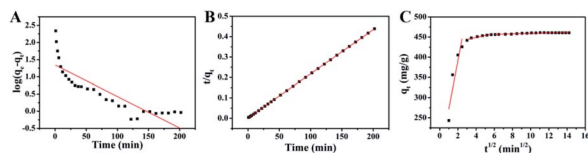| Temperature	Langmuir				Freundlich		
	q_{max} (mg g^{-1})	k_L (L mg^{-1})	R^2	R_L	k_F (mg$^{1-1/n}$ L$^{1/n}$ g^{-1})	$1/n$	R^2
275 K	598.80	1.893	0.99995	0.001758	415.715	7.143	0.90603
294 K	571.43	1.768	0.99941	0.001882	407.483	8.621	0.97103
313 K	564.97	1.475	0.99966	0.002255	395.440	8.333	0.95202

Fig. 5 (A) Pseudo-first-order model, (B) pseudo-second-order model, and (C) intraparticle diffusion model for the adsorption of MB onto S–N-rGO.

$$R_L = \frac{1}{1 + k_L C_0} \tag{4}$$

where the R_L value indicates that the Langmuir isotherms are favorable ($0 < R_L < 1$), unfavorable ($R_L > 1$), linear ($R_L = 1$) or irreversible ($R_L = 0$).[43] The R_L data (Table 2) demonstrated that S–N-rGO was a favorable adsorbent for MB adsorption. The Freundlich model supposes that the adsorption occurs on the medium surface in which adsorption sites are unevenly distributed. The linear equation is as follows:[44]

$$\ln q_e = \ln k_F + \frac{1}{n} \ln c_e \tag{5}$$

where k_F (mg$^{1-1/n}$ L$^{1/n}$ g^{-1}) is the Freundlich constant connected with the adsorption capacity and $1/n$ is the empirical parameter, which is associated with the adsorption intensity. k_F is determined by plotting $\ln q_e$ with a straight line relative to $\ln c_e$ (Fig. 4B), and the corresponding Freundlich isotherm constants

Table 3 Thermodynamic parameters for MB adsorbed by S–N-rGO

Kinetic model	Parameters	Values
Pseudo-first-order	K_1 (min^{-1})	0.0207
	q_e (mg g^{-1})	19.95
	R^2	0.7424
Pseudo-second-order	K_2 (g mg^{-1} min^{-1})	4.24×10^{-3}
	q_e (mg g^{-1})	462.96
	R^2	1.0000
Intraparticle diffusion model	K_{id1} (mg g^{-1} min$^{1/2}$)	120
	C_1 (mg g^{-1})	150
	R_1^2	0.8059
	K_{id2} (mg g^{-1} min$^{1/2}$)	4.90
	C_2 (mg g^{-1})	430
	R_2^2	0.9068
	K_{id3} (mg g^{-1} min$^{1/2}$)	0.580
	C_3 (mg g^{-1})	453
	R_3^2	0.8124

are listed in Table 2 after calculations. The low R^2 within the Freundlich model suggested that the adsorption data of MB onto S–N-rGO cannot be well fitted by the Freundlich model.

3.4 Kinetic studies

Adsorption kinetic studies were thoroughly explored at the condition of 294 K, since they can provide important information on the adsorption rate and mechanism. Fig. 5A and B show the pseudo-first-order and pseudo-second-order kinetics for the adsorption of MB onto S–N-rGO, respectively. These two kinetic models can be expressed in a linear form as follows:[45]

$$\log(q_e - q_t) = \log q_e - \frac{k_1}{2.303} t \tag{6}$$

where k_1 (min^{-1}) is the adsorption rate constant. The k_1 can be calculated through the fitting line by plotting $\log(q_e - q_t)$ *versus* t (Fig. 5A). The kinetic parameters were calculated, and the results are provided in Table 3. The determination coefficient was only 0.7424, indicating that the adsorption of MB onto S–N-rGO does not follow the pseudo-first-order kinetic model. The linear form of the pseudo-second-order model is expressed as follows:[46]

$$\frac{t}{q_t} = \frac{1}{k_2 q_e^2} + \frac{t}{q_e} \tag{7}$$

where k_2 (g mg^{-1} min) is the pseudo-second-order rate constant, and the value of k_2 was calculated by plotting t/q_t *versus* t fitting line (Fig. 5B). The determination coefficient (Table 3) was very high ($R^2 = 1.0000$) and the calculated equilibrium adsorption capacity (462.96 mg g^{-1}) was consistent with the experimental data (461.56 mg g^{-1}); therefore, the adsorption of MB onto S–N-rGO followed the pseudo-second-order kinetic model.

The steps of adsorption process are studied thoroughly with Weber's intraparticle diffusion model which is expressed as eqn (8).[47]

$$q_t = k_{id} t^{1/2} + C \tag{8}$$

where k_{id} (mg g^{-1} min$^{-1/2}$) is the intraparticle diffusion rate constant and C (mg g^{-1}) represents the intercept related to the adsorption steps. According to this model, a plot of q_t *versus* $t^{1/2}$ could be linear if intraparticle diffusion is involved in the adsorption process and if the plot passes through the origin, then intraparticle diffusion is the sole rate-limiting step.[48] It has also been suggested that in instances when q_t *versus* $t^{1/2}$ is multilinear, two or more steps govern the adsorption process.[49,50] Given the multilinearity of this plot for adsorption

Table 4 Thermodynamic parameters for MB adsorbed by S–N-rGO

T (K)	ΔG (kJ mol^{-1})	ΔH (kJ mol^{-1})	ΔS (J mol^{-1} K^{-1})
275	−10.160	−17.293	−25.940
294	−9.667	—	—
313	−9.174	—	—

of MB onto S–N-rGO, this suggested that adsorption occurred in three phases (Fig. 5C). The initial steeper section represented surface or film diffusion, the second linear section expressed a gradual adsorption stage where intraparticle or pore diffusion was rate-limiting and the third section was the final equilibrium stage. As the plot did not pass through the origin, intraparticle diffusion was not the only rate-limiting step. Thus, there were three processes controlling the adsorption rate, but only one was rate-limiting in any particular time range. The intraparticle diffusion rate constant k_{id} was calculated as shown in Fig. 5C and Table 3. Larger intercepts within the second and third stages suggested that the second and third stages had a larger role as the rate-limiting step.[51]

3.5 Thermodynamic study

To evaluate the effect of temperature on the adsorption process of MB onto S–N-rGO, the thermodynamic parameters such as Gibbs free energy (ΔG), enthalpy (ΔH) and entropy (ΔS) were calculated using the following equations:[52]

$$\Delta G = \Delta H - T\Delta S \qquad (9)$$

$$\ln\left(\frac{q_e}{C_e}\right) = -\frac{\Delta H}{RT} + \frac{\Delta S}{R} \qquad (10)$$

where R is the universal gas constant (8.314 J mol^{-1} K^{-1}). The values of ΔH and ΔS can be obtained from the slope and the intercept of the linear straight by the linear fitting plots of $\ln(q_e/c_e)$ *versus* $1/T$. The thermodynamic parameters at different temperatures are listed in Table 4. The values of ΔG were all negative, indicating that the adsorption reaction of MB onto S–N-rGO was a spontaneous process. As the temperature increased, the absolute value of ΔG became lower, which indicated that the higher the temperature, the more unfavorable the adsorption. The negative value of ΔH (−17.293 kJ mol^{-1}) suggested that the adsorption process of MB onto S–N-rGO was an exothermic process which was consistent with the effect of temperature.[53,54] The negative value of ΔS (−25.940 J mol^{-1} K^{-1}) corresponded to a decrease in the degree of freedom of the adsorbed species.[55]

4. Conclusions

In summary, novel S and N co-doped rGO hybrids have been successfully prepared by a one-step oil-bath heating method with GSH as a source of S and N. Adsorption experiments showed that the content of GSH had an effect on the adsorption capacity of MB onto S–N-rGO, and the best mass ratio between GO and GSH was determined to be 60 : 200, which can facilitate the efficient adsorption of MB from blue solutions turning into colorless within 2′07″. The effects of pH, temperature, contact time and adsorbent dose on the adsorption of MB onto S–N-rGO were studied in detail. The equilibrium adsorption data were more suitable for the Langmuir isotherm model and the adsorption capacity was 598.8 mg g^{-1} at 275 K. The kinetic study showed that the adsorption process followed the pseudo-second-order kinetic model. The intra-particle diffusion model studies indicated that kinetic adsorption involved three processes: surface or film diffusion, a gradual adsorption stage and final equilibrium stage. The thermodynamic parameters showed that the adsorption reaction was a spontaneous and exothermic process. The obtained results in this work indicated that the S–N-rGO hybrids can be used as potential candidates with high efficiency for removing MB from wastewaters.

Conflicts of interest

There are no conflicts of interest to declare.

Acknowledgements

References

1 J. Fu, Z. Chen, M. Wang, S. Liu, J. Zhang, J. Zhang, R. Han and Q. Xu, Adsorption of methylene blue by a high-efficiency adsorbent (polydopamine microspheres): kinetics, isotherm, thermodynamics and mechanism analysis, *Chem. Eng. J.*, 2015, **259**, 53–61.

2 K. Ai, Y. Liu, C. Ruan, L. Lu and G. Lu, Sp² C-Dominant N-Doped Carbon Sub-micrometer Spheres with a Tunable Size: A Versatile Platform for Highly Efficient Oxygen-Reduction Catalysts, *Adv. Mater.*, 2013, **25**, 998–1003.

3 L. Ai, J. Jiang and R. Zhang, Uniform polyaniline microspheres: a novel adsorbent for dye removal from aqueous solution, *Synth. Met.*, 2010, **160**, 762–767.

4 Z. Wu, H. Zhong, X. Yuan, H. Wang, L. Wang, X. Chen, G. Zeng and Y. Wu, Adsorptive removal of methylene blue by rhamnolipid-functionalized graphene oxide from wastewater, *Water Res.*, 2014, **67**, 330–344.

5 S.-T. Yang, S. Chen, Y. Chang, A. Cao, Y. Liu and H. Wang, Removal of methylene blue from aqueous solution by graphene oxide, *J. Colloid Interface Sci.*, 2011, **359**, 24–29.

6 H. Guo, T. Jiao, Q. Zhang, W. Guo, Q. Peng and X. Yan, Preparation of Graphene Oxide-Based Hydrogels as Efficient Dye Adsorbents for Wastewater Treatment, *Nanoscale Res. Lett.*, 2015, **10**, 272.

7 J. Dai, T. Huang, S.-q. Tian, Y.-j. Xiao, J.-h. Yang, N. Zhang, Y. Wang and Z.-w. Zhou, High structure stability and outstanding adsorption performance of graphene oxide aerogel supported by polyvinyl alcohol for waste water treatment, *Mater. Des.*, 2016, **107**, 187–197.

8 J.-G. Yu, L.-Y. Yu, H. Yang, Q. Liu, X.-H. Chen, X.-Y. Jiang, X.-Q. Chen and F.-P. Jiao, Graphene nanosheets as novel adsorbents in adsorption, preconcentration and removal of gases, organic compounds and metal ions, *Sci. Total Environ.*, 2015, **502**, 70–79.

9 W. Zhang, C. Zhou, W. Zhou, A. Lei, Q. Zhang, Q. Wan and B. Zou, Fast and Considerable Adsorption of Methylene Blue Dye onto Graphene Oxide, *Bull. Environ. Contam. Toxicol.*, 2011, **87**, 86.

10 W. Fan, W. Gao, C. Zhang, W. W. Tjiu, J. Pan and T. Liu, Hybridization of graphene sheets and carbon-coated Fe_3O_4 nanoparticles as a synergistic adsorbent of organic dyes, *J. Mater. Chem.*, 2012, **22**, 25108–25115.

11 Y. Guo, J. Deng, J. Zhu, X. Zhou and R. Bai, Removal of mercury(ii) and methylene blue from a wastewater environment with magnetic graphene oxide: adsorption kinetics, isotherms and mechanism, *RSC Adv.*, 2016, **6**, 82523–82536.

12 F. S. Omar, H. Nay Ming, S. M. Hafiz and L. H. Ngee, Microwave Synthesis of Zinc Oxide/Reduced Graphene Oxide Hybrid for Adsorption-Photocatalysis Application, *Int. J. Photoenergy*, 2014, **2014**, 8.

13 B. A. Bhanvase, T. P. Shende and S. H. Sonawane, A review on graphene–TiO_2 and doped graphene–TiO_2 nanocomposite photocatalyst for water and wastewater treatment, *Environ. Technol. Rev.*, 2017, **6**, 1–14.

14 J. Dai, J. Yuan and P. Giannozzi, Gas adsorption on graphene doped with B, N, Al, and S: A theoretical study, *Appl. Phys. Lett.*, 2009, **95**, 232105.

15 L. Feng, Z. Qin, Y. Huang, K. Peng, F. Wang, Y. Yan and Y. Chen, Boron-, sulfur-, and phosphorus-doped graphene for environmental applications, *Sci. Total Environ.*, 2020, **698**, 134239.

16 P. A. Denis, Lithium adsorption on heteroatom mono and dual doped graphene, *Chem. Phys. Lett.*, 2017, **672**, 70–79.

17 P. A. Denis, C. P. Huelmo and F. Iribarne, Theoretical characterization of sulfur and nitrogen dual-doped graphene, *Comput. Theor. Chem.*, 2014, **1049**, 13–19.

18 L. Zhao, B. Yu, F. Xue, J. Xie, X. Zhang, R. Wu, R. Wang, Z. Hu, S. Yang and J. Luo, Facile hydrothermal preparation of recyclable S-doped graphene sponge for Cu^{2+} adsorption, *J. Hazard. Mater.*, 2015, **286**, 449–456.

19 Q. Luo, F. Hao, S. Wang, H. Shen, L. Zhao, J. Li, M. Grätzel and H. Lin, Highly efficient metal-free sulfur-doped and nitrogen and sulfur dual-doped reduced graphene oxide counter electrodes for dye-sensitized solar cells, *J. Phys. Chem. C*, 2014, **118**, 17010–17018.

20 Y. Su, Y. Zhang, X. Zhuang, S. Li, D. Wu, F. Zhang and X. Feng, Low-temperature synthesis of nitrogen/sulfur co-doped three-dimensional graphene frameworks as efficient metal-free electrocatalyst for oxygen reduction reaction, *Carbon*, 2013, **62**, 296–301.

21 Y. Tian, Y. Ma, H. Liu, X. Zhang and W. Peng, One-step and rapid synthesis of nitrogen and sulfur co-doped graphene for hydrogen peroxide and glucose sensing, *J. Electroanal. Chem.*, 2015, **742**, 8–14.

22 X. Wu, Z. Xie, M. Sun, T. Lei, Z. Zuo, X. Xie, Y. Liang and Q. Huang, Edge-rich and (N, S)-doped 3D porous graphene as an efficient metal-free electrocatalyst for the oxygen reduction reaction, *RSC Adv.*, 2016, **6**, 90384–90387.

23 B. Feng, J. Xie, C. Dong, S. Zhang, G. Cao and X. Zhao, From graphite oxide to nitrogen and sulfur co-doped few-layered graphene by a green reduction route via Chinese medicinal herbs, *RSC Adv.*, 2014, **4**, 17902–17907.

24 X. Duan, K. O'Donnell, H. Sun, Y. Wang and S. Wang, Sulfur and nitrogen co-doped graphene for metal-free catalytic oxidation reactions, *Small*, 2015, **11**, 3036–3044.

25 J. Liang, Y. Jiao, M. Jaroniec and S. Z. Qiao, Sulfur and nitrogen dual-doped mesoporous graphene electrocatalyst for oxygen reduction with synergistically enhanced performance, *Angew. Chem., Int. Ed.*, 2012, **51**, 11496–11500.

26 B. Liu, X. Ren, L. Chen, X. Ma, Q. Chen, Q. Sun, L. Zhang, P. Si and L. Ci, High efficient adsorption and storage of iodine on S, N co-doped graphene aerogel, *J. Hazard. Mater.*, 2019, **373**, 705–715.

27 N. I. Kovtyukhova, P. J. Ollivier, B. R. Martin, T. E. Mallouk, S. A. Chizhik, E. V. Buzaneva and A. D. Gorchinskiy, Layer-by-layer assembly of ultrathin composite films from micron-sized graphite oxide sheets and polycations, *Chem. Mater.*, 1999, **11**, 771–778.

28 D. Geng, Y. Chen, Y. Chen, Y. Li, R. Li, X. Sun, S. Ye and S. Knights, High oxygen-reduction activity and durability of nitrogen-doped graphene, *Energy Environ. Sci.*, 2011, **4**, 760–764.

29 L. Lai, J. R. Potts, D. Zhan, L. Wang, C. K. Poh, C. Tang, H. Gong, Z. Shen, J. Lin and R. S. Ruoff, Exploration of the active center structure of nitrogen-doped graphene-based catalysts for oxygen reduction reaction, *Energy Environ. Sci.*, 2012, **5**, 7936–7942.

30 N. A. Kumar, H. Nolan, N. McEvoy, E. Rezvani, R. L. Doyle, M. E. G. Lyons and G. S. Duesberg, Plasma-assisted simultaneous reduction and nitrogen doping of graphene oxide nanosheets, *J. Mater. Chem. A*, 2013, **1**, 4431–4435.

31 S. Yang, L. Zhi, K. Tang, X. Feng, J. Maier and K. Müllen, Efficient synthesis of heteroatom (N or S)-doped graphene based on ultrathin graphene oxide-porous silica sheets for oxygen reduction reactions, *Adv. Funct. Mater.*, 2012, **22**, 3634–3640.

32 X. Wang, J. Wang, D. Wang, S. Dou, Z. Ma, J. Wu, L. Tao, A. Shen, C. Ouyang, Q. Liu and S. Wang, One-pot synthesis of nitrogen and sulfur co-doped graphene as efficient metal-free electrocatalysts for the oxygen reduction reaction, *Chem. Commun.*, 2014, **50**, 4839–4842.

33 D. Wang, S. H. Vijapur and G. G. Botte, Coal char derived few-layer graphene anodes for lithium ion batteries, *Photonics*, 2014, **1**, 251–259.

34 M. S. Sher Shah, K. Zhang, A. R. Park, K. S. Kim, N. G. Park, J. H. Park and P. J. Yoo, Single-step solvothermal synthesis of mesoporous Ag-TiO_2-reduced graphene oxide ternary composites with enhanced photocatalytic activity, *Nanoscale*, 2013, **5**, 5093–5101.
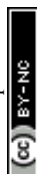
35 Y. Xu, H. Bai, G. Lu, C. Li and G. Shi, Flexible graphene films via the filtration of water-soluble noncovalent functionalized graphene sheets, *J. Am. Chem. Soc.*, 2008, **130**, 5856–5857.

36 H. L. Guo, X. F. Wang, Q. Y. Qian, F. B. Wang and X. H. Xia, A green approach to the synthesis of graphene nanosheets, *ACS Nano*, 2009, **3**, 2653–2659.

37 B. Sarmento, D. Ferreira, F. Veiga and A. Ribeiro, Characterization of insulin-loaded alginate nanoparticles produced by ionotropic pre-gelation through DSC and FTIR studies, *Carbohydr. Polym.*, 2006, **66**, 1–7.

38 N. Song, X.-L. Wu, S. Zhong, H. Lin and J.-R. Chen, Biocompatible $G\text{-}Fe_3O_4/CA$ nanocomposites for the removal of Methylene Blue, *J. Mol. Liq.*, 2015, **212**, 63–69.

39 R. Aravindhan, N. N. Fathima, J. R. Rao and B. U. Nair, Equilibrium and thermodynamic studies on the removal of basic black dye using calcium alginate beads, *Colloids Surf., A*, 2007, **299**, 232–238.

40 L. Chen, Y. Li, Q. Du, Z. Wang, Y. Xia, E. Yedinak, J. Lou and L. Ci, High performance agar/graphene oxide composite aerogel for methylene blue removal, *Carbohydr. Polym.*, 2017, **155**, 345–353.

41 L. Li, L. Fan, M. Sun, H. Qiu, X. Li, H. Duan and C. Luo, Adsorbent for hydroquinone removal based on graphene oxide functionalized with magnetic cyclodextrin–chitosan, *Int. J. Biol. Macromol.*, 2013, **58**, 169–175.

42 E. Bulut, M. Özacar and İ. A. Şengil, Equilibrium and kinetic data and process design for adsorption of Congo Red onto bentonite, *J. Hazard. Mater.*, 2008, **154**, 613–622.

43 K. Zhou, Y. Li, L. Qi, Q. Du and Y. Xia, Kinetic, isotherm and thermodynamic studies for removal of methylene blue using β-cyclodextrin/activated carbon aerogels, *J. Polym. Environ.*, 2018, **26**, 1–9.

44 V. K. Gupta, D. Pathania, S. Sharma, S. Agarwal and P. Singh, Remediation and recovery of methyl orange from aqueous solution onto acrylic acid grafted Ficus carica fiber: isotherms, kinetics and thermodynamics, *J. Mol. Liq.*, 2013, **177**, 325–334.

45 M. Doğan, M. Alkan, Ö. Demirbaş, Y. Özdemir and C. Özmetin, Adsorption kinetics of maxilon blue GRL onto sepiolite from aqueous solutions, *Chem. Eng. J.*, 2006, **124**, 89–101.

46 Y. S. Ho and C. C. Chiang, Sorption Studies of Acid Dye by Mixed Sorbents, *Adsorption*, 2001, **7**, 139–147.

47 L. Chen and B. Bai, Equilibrium, Kinetic, Thermodynamic, and in Situ Regeneration Studies about Methylene Blue Adsorption by the Raspberry-like TiO_2@yeast Microspheres, *Ind. Eng. Chem. Res.*, 2013, **52**, 15568–15577.

48 A. Ozcan, A. Ozcan and O. Gok, Adsorption kinetics and isotherms of anionic dye of reactive blue 19 from aqueous solutions onto DTMA-sepiolite, *Hazardous Materials and Wastewater—Treatment, Removal and Analysis*, Nova Science Publishers, New York, 2007.

49 E. I. Unuabonah, K. O. Adebowale and B. I. Olu-Owolabi, Kinetic and thermodynamic studies of the adsorption of lead (II) ions onto phosphate-modified kaolinite clay, *J. Hazard. Mater.*, 2007, **144**, 386–395.

50 F.-C. Wu, R.-L. Tseng and R.-S. Juang, Initial behavior of intraparticle diffusion model used in the description of adsorption kinetics, *Chem. Eng. J.*, 2009, **153**, 1–8.

51 H. K. Boparai, M. Joseph and D. M. O'Carroll, Kinetics and thermodynamics of cadmium ion removal by adsorption onto nano zerovalent iron particles, *J. Hazard. Mater.*, 2011, **186**, 458–465.

52 P. K. Neghlani, M. Rafizadeh and F. A. Taromi, Preparation of aminated-polyacrylonitrile nanofiber membranes for the adsorption of metal ions: comparison with microfibers, *J. Hazard. Mater.*, 2011, **186**, 182–189.

53 N. Nasuha and B. H. Hameed, Adsorption of methylene blue from aqueous solution onto NaOH-modified rejected tea, *Chem. Eng. J.*, 2011, **166**, 783–786.

54 H. Li, D. Zhang, X. Han and B. Xing, Adsorption of antibiotic ciprofloxacin on carbon nanotubes: pH dependence and thermodynamics, *Chemosphere*, 2014, **95**, 150–155.

55 A. Özcan, E. M. Öncü and A. S. Özcan, Kinetics, isotherm and thermodynamic studies of adsorption of Acid Blue 193 from aqueous solutions onto natural sepiolite, *Colloids Surf., A*, 2006, **277**, 90–97.